Three-dimensional multifluid simulations of ionospheric loss at Mars from nominal solar wind conditions to magnetic cloud events

E. M. Harnett[1] and R. M. Winglee[1]

Received 14 March 2006; revised 23 June 2006; accepted 30 June 2006; published 21 September 2006.

[1] Three-dimensional multifluid simulations of the solar wind interaction with a magnetized Mars are used to determine both the effect of the crustal magnetic field on ionospheric loss rate and the ionospheric loss rate as a function of solar wind conditions. Ionospheric losses on the order of 10^{25} O_2^+ ions per second are found for quiet solar wind conditions. This is of the same order as that estimated from Phobos 2 measurements. Varying the orientation of Mars' magnetic anomalies relative to the incident solar wind direction leads to only minor variation in the ionospheric loss rates of O_2^+ for each set of solar wind conditions studied. Solar wind parameters were varied from nominal solar wind conditions to conditions with high-speed flows, high densities, and large IMF magnitudes. Outflow rates on the order of 10^{26} O_2^+ ions per second were seen for storm-like conditions. The simulations indicate that ionospheric outflow rates increase by a larger percentage for high solar wind number density when compared to high solar wind speed or strong IMF conditions alone. This is due to the higher solar wind density and temperature of the precipitating ions. The results also indicate a significant influence of pickup on ionospheric loss.

Citation: Harnett, E. M., and R. M. Winglee (2006), Three-dimensional multifluid simulations of ionospheric loss at Mars from nominal solar wind conditions to magnetic cloud events, *J. Geophys. Res.*, *111*, A09213, doi:10.1029/2006JA011724.

1. Introduction

[2] Understanding the loss of the Martian atmosphere is central not only in the study of the interaction of the current day Mars with the solar wind, but also in determining to how much water and CO_2 Mars may have lost to space in the past. Prior to about 3.5 billion years ago, impacts likely removed 50–90% of the early atmosphere [*Brain and Jakosky*, 1998]. However, this mechanism is not mass selective, and thus after the era of large impacts ceased, another mechanism for loss must have taken over to produce the isotopic fractionization measured in the current atmosphere (for a review, see *Jakosky and Phillips* [2001]). Atomic hydrogen can escape directly into space, as it is not gravitationally bound, but for heavier neutrals other loss mechanisms will dominate. Dissociative recombination of O_2^+ is the dominant process in creating escaping oxygen [*Zhang et al.*, 1993]. If formed near the exobase, this nonthermal oxygen can escape to form the hot oxygen corona [*Nagy and Cravens*, 1988].

[3] Forcing by the solar wind on the ionospheric plasma produces another main loss mechanism. Measurements by Phobos 2 indicate significant amounts of oxygen and molecular species are currently being scoured from the atmosphere by the solar wind [e.g., *Lundin et al.*, 1990]. O^+ ion beams dominate the central tail, while the flank region is dominated by O^+ and, at times, by either O_2^+ or CO_2^+ [*Lundin et al.*, 1989]. Analysis by *Kallio et al.* [1995] showed that the O^+ population in the tail formed both a steady outflow of O^+ in the Martian optical shadow, and a high energy O^+ population outside of the optical shadow which is possibly the result of a dynamical process in the tail. Furthermore, the regions of tail-streaming oxygen ions corresponded with a reduction in the flux of H^+ and the flow velocity [*Lundin et al.*, 1989; *Verigin et al.*, 1991a].

[4] The exact mechanism for ions flows in the tail and rates of escape are still not well constrained. Estimates from Phobos 2 measurements made near solar maximum place the loss rate of O^+ at 3×10^{25} ions s^{-1} [*Lundin et al.*, 1989; *Rosenbauer et al.*, 1989]. Previous calculations of atmospheric loss rates have primarily assumed no planetary magnetic field. Table 1 contains a sample of loss rates calculated from different types of models. A more complete list is given by *Lammer et al.* [2003]. The values show that estimates based on 1-D models are typically an order of magnitude larger than from both 3-D test particle simulation and self-consistent fluid models, with the 3-D simulations being closest to estimates from Phobos 2 data. 1-D simulations cannot capture the complex plasma flows that can develop around a planet. Measurements at Venus showed ion flows out of the dayside ionosphere that converged into surface flows on the nightside [e.g., *Knudsen*, 1992]. *Shinagawa and Cravens* [1989] found that the solar wind

[1]Department of Earth and Space Sciences, University of Washington, Seattle, Washington, USA.

0148-0227/06/2006JA011724

Table 1. Ionospheric Loss Rates[a]

Source	Escape Rate, atoms s^{-1}
Lundin et al. [1989], Phobos 2	3×10^{25} (O^+)
Luhmann et al. [1992], 1-D Model	8×10^{25} (O)
Kar et al. [1996], 1-D model	4×10^{26} (O_2^+)
Fox [1997], 1-D model	1×10^{25}(O^+), 7×10^{25} (O_2^+)
Luhmann and Kozyra [1991], 3-D test	10^{23}(O^+), $\times 10^{25}$ (O)
Kallio and Koskinen [1999], 3-D test	2×10^{25}(O^+)
Kallio and Janhunen [2002], 3-D model	$10^{24} - 10^{25}$(O^+)
Ma et al. [2002], 3-D model	4×10^{24}(O^+), 2×10^{25} (O_2^+)
Ma et al. [2004], 3-D model	9×10^{23}(O^+), 1×10^{24} (O_2^+)

[a]All 1-D models assume an unmagnetized Mars. The 3-D models by *Ma et al.* [2002, 2004] incorporated the anomalous magnetic field. The numbers listed are for nominal solar wind conditions. The simulations by *Luhmann and Kozyra* [1991] and *Kallio and Koskinen* [1999] used test particles to estimate a global loss rate. Where the models distinguish between solar min and solar max, the loss rates for solar min have been given.

interaction with the upper Martian ionosphere could lead to large horizontal plasma motions in their model. Using a photochemical equilibrium model to produce a 1-D profile of production rates and density at both solar minimum and solar maximum, *Fox* [1997] found that the 1-D nature of their model overestimated loss rates, as it could not account for horizontal transport of ions. *Fox* [1997] theorized that something similar to the converging plasma flow on the nightside of Venus could occur at Mars. Observations of asymmetric and convergent flows indicate that 3-D models are necessary to gain a complete picture of the dynamics of the system.

[5] Loss of atmosphere through solar wind interactions is controlled by the composition and extent of the atmosphere, chemical processes in the atmosphere, the solar wind conditions and the presence of a planetary magnetic field. Three-dimensional test particle simulations by *Luhmann and Korzya* [1991] indicated that loss from the atmosphere to form the hot oxygen corona and sputtering by pickup ions were the dominate loss mechanisms for atmospheric oxygen, with the loss rates of both processes $\sim 4 \times 10^{24} - 2 \times 10^{25}$ s^{-1}. Loss due to direct solar wind pickup of the ionosphere was two orders of magnitude smaller. Using a 3-D hybrid model, *Kallio and Janhunen* [2002] found the the loss rate of oxygen could vary from 10^{24} s^{-1} to 10^{25} s^{-1} depending on the presence of a thick corona and the ion production rate within the ionosphere and corona. Increasing the ion production rate by a factor of four increased the loss rate by a factor of three.

[6] As the Martian dynamo appears to have ceased prior to the era of heavy bombardment [*Acuna et al.*, 2001], the crustal magnetic fields would have been the only source of planetary magnetic field to modulate the loss of ionosphere during the period when the ionospheric interaction with the solar wind dominated the loss processes. Observations using both radio occultation from MGS [*Ness et al.*, 2000] and the MAG/ER instrument on MGS [*Mitchell et al.*, 2001] showed that the magnetic anomalies influence the structure of the ionosphere. *Ness et al.* [2000] found regions where the crustal magnetic field is mostly radial, producing cusp-like structures. The solar wind can flow into these regions, heating the atmosphere and inflating it. *Mitchell et al.* [2001] found regions of closed magnetic field lines, or "plasma voids", that were protected from the solar wind by magnetic fields associated with the magnetic anomalies. They also found that successive plasma voids would be separated by regions of plasma with an energy spectrum similar to the hot, magnetosheath plasma, indicating that the magnetic field lines were once connected to the IMF. These cusp-like structures have lateral sizes in excess of 2000 km, producing an extended region over which the ionosphere is heated and partially lost to the solar wind. Thus the anomalous magnetic field can potentially create extended regions where solar wind forcing is substantially reduced or increased, as compared to unmagnetized regions.

[7] Recent observations by Mars Express (MEX), taken near solar minimum, have shown that while solar wind protons were typically not seen below an altitude of 500 km, solar wind forcing of the ionosphere is measured down to an altitude of at least 270 km (the periapsis of the satellite) [*Lundin et al.*, 2004]. Also, on at least one occasion, flux measurements suggest that solar wind hydrogen ions with energies on the order of several keV were penetrating down to 290 km. They also saw indication that the solar wind forcing of the upper atmosphere may be modulated by the magnetic anomalies, suggesting that the anomalies may play some role in the atmospheric loss.

[8] *Leblanc et al.* [2002] looked at the effect of solar energetic particles (SEP) on the Martian atmosphere using 3-D particle tracking. They used the magnetic and electric fields generated from a 3-D MHD model of the Martian magnetosphere for quiet solar wind conditions as the basis for the particle tracking. They found that SEP hydrogen ions do not significantly increase the atmospheric escape flux. However, SEP oxygen ions substantially increase the escape flux due to the fact that the oxygen SEPs can sputter the Martian atmosphere much more effectively than hydrogen SEPs. When including the crustal magnetic field, they found that some regions of anomalous magnetic field could completely prevent precipitation of SEPs with energy less than 83 MeV, but those SEPs deflected from regions of high anomalous magnetic field were funneled into nearby regions. This meant that the surface flux in the regions that the SEPs were funneled into was larger than the background flux at unmagnetized regions. This process of deflection and funneling lead to little change in the net SEP flux at the surface. Therefore they indicate that the magnetic anomalies would only have a small effect on the net escape flux generated by these high-energy solar particles.

[9] *Ma et al.* [2002, 2004] calculated loss rates from the Martian atmosphere using 3-D MHD simulations that included a magnetized Mars for more than one solar wind configuration and both solar minimum and solar maximum conditions. The model is capable of tracking different ion populations, but assumes all the ion species have the same velocity and temperature. The more recent simulations [*Ma et al.*, 2004] produced ionospheric profiles similar to that measured by the Viking landers for solar min conditions but found escape fluxes one to two orders of magnitude smaller than those estimated from Phobos 2 measurements depending on the conditions assumed. The loss rates listed for this model in Table 1 are for the case matching the Viking lander profile.

[10] After the era of heavy bombardment and the global dipole field ceased (3.9 to 3.5 Gya), and solar wind driven

loss mechanisms became significant, the X-ray to UV flux from the Sun was probably 3–50 times stronger [*Ribas et al.*, 2005], while the solar wind speed was on the order of four times stronger [*Newkirk*, 1980; *Lammer et al.*, 2003] and the solar wind density was 15 to 40 times larger [*Wood et al.*, 2002; *Lammer et al.*, 2003]. The X-ray to XUV flux of a current day active Sun is 10–100 times that of a quiet Sun, while the EUV to UV flux is only slightly more intense or the same as that of the quiet Sun [*Smith and Gottlieb*, 1974]. However, a B class flare (the most common type [*Dennis*, 1988]) can have X-ray and XUV fluxes 10^3 to 10^5 times that of the quiet Sun and EUV to UV fluxes 10 times that of the quiet Sun [*Smith and Gottlieb*, 1974]. A statistical study of 549 solar storms indicated that during intense storms the solar wind density at the Earth is, on average 28 cm^{-3} while the speed is 500 km s^{-1} [*Zhang et al.*, 2006]. This density scales to 6 times the nominal density (of 2 cm^{-3}) at Mars. While the solar wind speed and density during current day storms may not reach the possible upper limits for an early Sun as a group, the density or speed from individual storms do come close. For example, during the 2003 Halloween storm, solar wind speeds on the order of 2000 km s^{-1} were measured [*Skoug et al.*, 2004], five times the nominal solar wind speed. During the January 1997 event, a solar wind density on the order of 150 cm^{-3} was measured near the Earth [*Burlaga et al.*, 1998], 30 times the nominal solar wind density. This suggests that current day storms can be used as analogs for early Sun conditions, allowing model results to be tested against data for intervals when solar wind conditions are not current day nominal values. This is important as loss rates may not vary linearly with changes in different solar wind parameters. Looking at a variety of solar wind conditions can shed light both on how loss rates may have varied over time and the effectiveness of the magnetic anomalies in protecting the ionosphere and the surface from the solar wind during current storm conditions. It is also important to know the size of any regions protected by the anomalous magnetic field, and whether those regions are transient, either moving around or disappearing altogether for different solar wind conditions and orientations of the planet relative to the incident solar wind direction.

[11] This paper presents results from 3-D multifluid simulations of the solar wind interaction with a magnetized Mars for a variety of anomalous magnetic field orientations and solar wind conditions. The case of the strong southern magnetic anomalies located at the noon meridian is analyzed in detail in order to discuss the physical processes occurring during storm conditions. The paper then discusses how the location of the anomalous magnetic field modulates ionospheric loss rates and how those loss rates scale with solar wind density, solar wind speed and IMF strength.

2. Model

[12] Any number of species and populations can be assumed in the model, with the limits being computation speed. For the results presented below, two ion populations were used, a hydrogen solar wind population and either ionospheric O_2^+ or O^+ population. The model solves the following equations in 3-D on a nested grid system. The coordinates are such that $\vec{z}$ is perpendicular to the ecliptic plane, $\vec{y}$ is in the ecliptic plane but perpendicular to the solar wind velocity, and $\vec{x}$ is in the same direction as the solar wind bulk velocity. The three grids were centered on the z axis about the equator, and on the y axis about the noon meridian. The grids were placed along the x axis such that the bow shock did not form near a box boundary. The resolution of the finest grid is equal to 109 km near the surface, increasing to 435 km out in the solar wind. The simulation area ranges from 4.5 R_M upstream to 5 R_M downtail; The area ranges between 5–6 R_M over both the poles and 6–7 R_M on the dawn and dusk flanks, depending on the orientation of the IMF and the size of the magnetosphere. Detailed descriptions of the multifluid technique are given by *Winglee* [2004]. The multifluid equations are:

$$\frac{\partial \rho_i^{\mathrm{m}}}{\partial t} + \nabla \cdot \left(\rho_i^{\mathrm{m}} \mathbf{v}_i\right) = 0 \tag{1}$$

$$\rho_i^{\mathrm{m}} \frac{\mathrm{d}\mathbf{v}_{\mathrm{i}}}{\mathrm{dt}} = q_i n_i (\mathbf{E} + \mathbf{v}_i \times \mathbf{B}) - \nabla \mathrm{P_i} + \rho_{\mathrm{i}}^{\mathrm{m}} \mathbf{g}(\mathbf{r}) \tag{2}$$

$$\frac{\partial \mathrm{P_i}}{\partial t} = -\gamma \nabla \cdot (\mathrm{P_i} \mathbf{v_i}) + (\gamma - 1)\mathbf{v_i} \cdot \nabla \mathrm{P_i} \tag{3}$$

$$\frac{\partial \mathrm{P_e}}{\partial t} = -\gamma \nabla \cdot (\mathrm{P_e} \mathbf{v_{de}}) + (\gamma - 1)\mathbf{v_{de}} \cdot \nabla \mathrm{P_e} \tag{4}$$

$$\frac{\partial \mathbf{B}}{\partial t} + \nabla \times \mathbf{E} = 0 \tag{5}$$

$$\mathbf{J} = \frac{1}{\mu_o} \nabla \times \mathbf{B} \tag{6}$$

$$n_e = \sum_i n_i \tag{7}$$

$$\mathbf{v}_{de} = \sum_i \frac{n_i}{n_e} \mathbf{v}_i - \frac{\mathbf{J}}{e n_e} \tag{8}$$

$$\mathbf{E} = -\sum_i \frac{n_i}{n_e} \mathbf{v}_i \times \mathbf{B} + \eta \mathbf{J} + \frac{1}{e n_e} (\mathbf{J} \times \mathbf{B} - \nabla \mathrm{P_e}) \tag{9}$$

where ρ_i^{m} is the ion mass density, n_i the ion number density, q_i ion charge, $\mathbf{v}_i$ the ion bulk velocity, and P_i the ion pressure, of each individual ion species i. P_e is the electron pressure. This ratio of electron temperature to ion temperature is initialized at 0.5 but then allowed to vary with time at all locations. The electron number density is n_e, and $\mathbf{v}_{de}$ is the electron drift speed. $\mathbf{g}(\mathbf{r})$ is the gravitational vector, $\mathbf{J}$ is the current density, $\mathbf{B}$ is the magnetic field, and $\mathbf{E}$ is the electric field. γ is the ratio of specific heats and equal to $\frac{5}{3}$. The resistivity (η) is nonzero only inside the inner boundary and the Hall and $\nabla \mathrm{P}_e$ terms are only evaluated outside the inner boundary. The inner boundary is the spherical surface representing the planet. The pressure,

Table 2. Solar Wind Parameters[a]

	Solar Wind Density	Solar Wind Speed	IMF Strength	IMF Direction	Difference From Case A
Case A	2 cm^{-3}	400 km s^{-1}	2 nT	B_y	-
Case B	2 cm^{-3}	800 km s^{-1}	2 nT	B_y	$2 \times v_{sw}$
Case C	2 cm^{-3}	400 km s^{-1}	2 nT	B_z	IMF rot.
Case D	12 cm^{-3}	400 km s^{-1}	2 nT	B_y	$6 \times n_{sw}$
Case E	12 cm^{-3}	800 km s^{-1}	2 nT	B_y	$6 \times n_{sw}$, $2 \times v_{sw}$
Case F	12 cm^{-3}	400 km s^{-1}	6 nT	B_y	$6 \times n_{sw}$, $3 \times$ IMF
Case G	40 cm^{-3}	400 km s^{-1}	6 nT	B_y	$20 \times n_{sw}$, $3 \times$ IMF
Case H[b]	2 cm^{-3}	400 km s^{-1}	2 nT	B_y	$m_{ion}/2$

[a]In cases A-G the ionosphere was assumed to be O_2^+, with a mass of 32 m_p.
[b]In case H the mass of the ionospheric ion was reduced by half to simulate an ionosphere composed primarily of O^+ instead.

density, momentum and anomalous magnetic field are all held constant inside this surface while the finite resistivity of the region allows for diffusion of a small amount of the IMF, which is consistent with the high, but not infinite, conductivity of the ionosphere. Outside of this region the resistivity is zero, and the plasma is collisionless.

[13] Substituting Ohm's law (equation (9)) into the momentum equation (equation (2)) yields:

$$\rho_i^{\mathrm{m}} \frac{\mathrm{d}\mathbf{v}_{\mathrm{i}}}{\mathrm{dt}} = q_i n_i \left(\mathbf{v}_i \times \mathbf{B} - \sum_\alpha \frac{n_\alpha}{n_e} \mathbf{v}_\alpha \times \mathbf{B} \right) + q_i n_i \left(\frac{\mathbf{J} \times \mathbf{B}}{e n_e} - \frac{\nabla \mathrm{P_e}}{e n_e} \right) - \nabla \mathrm{P_i} + \rho_{\mathrm{i}}^{\mathrm{m}} \mathbf{g}(\mathbf{r}) \tag{10}$$

If one assumes either a single species or a single velocity for all the species, then the difference

$$\mathbf{v}_i \times \mathbf{B} - \sum_\alpha \frac{n_\alpha}{n_e} \mathbf{v}_\alpha \times \mathbf{B} \tag{11}$$

is zero and equation (10) reduces to the corresponding MHD Ohm's law. However, in the presence of different ion species or energy populations, this difference is invariably nonzero and is what drives ion cyclotron effects. This is the reason that these multifluid simulations can model such features as an asymmetric bow shock due to ionospheric ion pickup. The same difference occurs in hybrid simulations where there is a difference in the velocity of the individual ions relative to the bulk velocity, which is derived from a sum similar to the one in equation (10). This makes the results from this model similar to those from hybrid simulations of the solar wind interaction with Mars by *Brecht* [1997a]. A more extensive discussion and comparison between this multifluid model and a hybrid model are given by *Harnett et al.* [2005].

[14] The Parker spiral approximation of the direction of the IMF at Mars' orbit puts the magnitude of the B_y component 1.5 times larger than the B_x component. Various measurements of solar wind parameters by Phobos 2 and MGS show the magnitude of the IMF in the range of 2–3 nT, and confirm that the B_y component is typically larger than the B_x component [cf.*Kallio et al.*, 1995; *Vignes et al.*, 2000]. In the results discussed below, the magnitude of the IMF is varied between 2 nT and 6 nT, in either the B_y or B_z direction. Looking at only a single component for each run allows for the investigation of the dependence of the outflow rate on IMF orientation. Also *Brecht* [1997b] showed, using hybrid simulations, that a perpendicular shock orientation (i.e IMF in B_y or B_z) leads to a lower bound on the estimate of the solar wind precipitation into the exobase.

[15] The model of the Martian magnetic field was provided by *Cain et al.* [2003]. A 90 term internal potential function was generated using 110,000 three-component observations from MGS. For the results presented, the equatorial plane of Mars is aligned with the ecliptic plane. The simulations were run to steady state conditions for a given orientation of the intrinsic magnetic field, as the time to reach steady state is negligible in comparison to Mars' rotational period. The surface magnetic field was only rotated between simulation runs. The region of strong southern magnetic anomalies (SSMAs) was located at the noon and midnight meridian, and the dawn and dusk terminators.

[16] For quiet conditions, the solar wind (i.e. hydrogen) density is set equal to 2 ions cm^{-3}, and a bulk speed of 400 km s^{-1}, with a thermal energy of 10 eV. To simulate storm (or active Sun) conditions, the solar wind density is increased to 12 ions cm^{-3} and the bulk speed set to 800 km s^{-1}. The storm time density is determined by scaling a value of 20 ions cm^{-3} at the Earth to Mars' orbit [cf. *Tsyganenko and Sitnov*, 2005; *Richardson et al.*, 2005]. The solar wind parameters for each case studied are summarized in Table 2.

[17] Viking 1 measured O_2^+ to be the predominant ion species below 300 km. The density at 300 km was 200–400 cm^{-3}, while the maximum O_2^+ density of 10^5 cm^{-3} occurred at 130 km from the surface [*Hanson et al.*, 1977]. These measurements were made near solar minimum and thus represent a lower bound for ionospheric densities. The inner boundary is defined to be at an altitude of 300 km, as this is well above the exobase (which forms at about 175 km [*Luhmann et al.*, 1992]). At and below the exobase collisional processes, which are not included in the model, will become important. The O_2^+ number density at the inner boundary is held fixed at 400 cm^{-3}. The initial ionospheric density then falls off with a scale height of 100 km. A scale height of approximately 60 km can be derived from the Viking density profiles, but the finest resolution of the simulations is 100 km, thereby setting the scale height. The temperature at the inner boundary is held fixed at 3000 K per the Viking measurements [*Hanson et al.*, 1977], allowing for a thermal velocity. The ions at the inner boundary are assumed to have no bulk

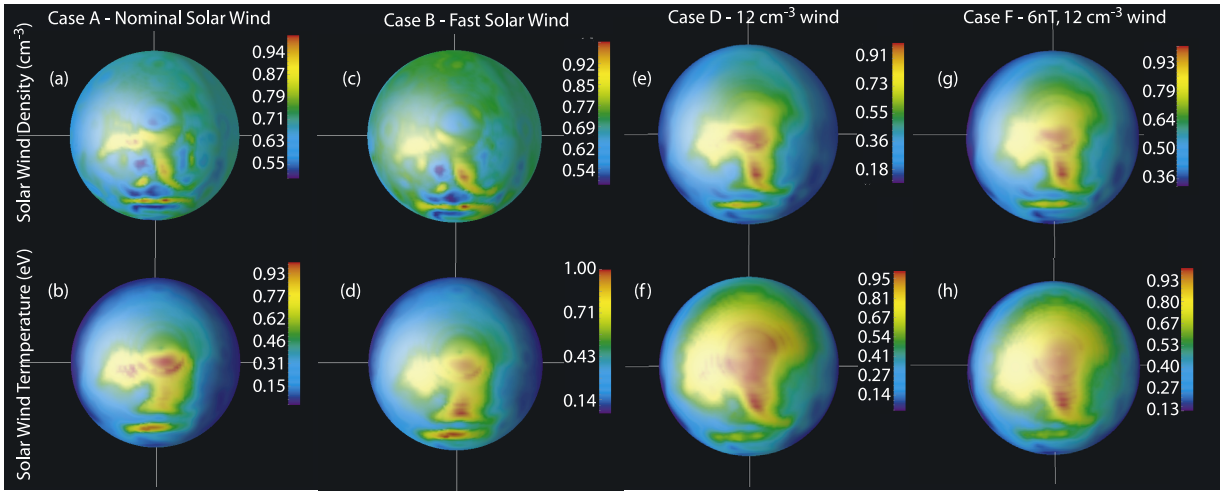

Figure 1. Solar wind density and temperature on the dayside at an altitude of 400 km (100 km, or one grid point, above the planetary boundary) when the SSMAs are located at noon for cases A, B, D, and F. The color bars are in normalized units such that the maximum value is 1.0. The minimum values vary with each image. The normalizing factors for the color bars are (a) 1.27 cm^{-3}, (b) 32.3 eV, (c) 1.30 cm^{-3}, (d) 140 eV, (e) 5.50 cm^{-3}, (f) 148 eV, (g) 2.80 cm^{-3}, and (h) 75.0 eV.

velocity. The night side ionospheric number density at the inner boundary is reduced to 40 cm^{-3} to simulate the reduced nightside ion density that comes about from no UV flux. Further discussion of the affect of changes in the nightside ion density on the model is given by *Harnett and Winglee* [2005].

[18] In the analysis, the subsolar point of the bow shock and the magnetic pileup boundary for each set of solar wind conditions will be noted, thus indicating changes in the size and shape of the magnetosphere. The standoff distance of the bow shock has been calculated to be between 1.47 R_M and 1.62 R_M using Phobos 2 observations near solar maximum [*Trotignon et al.*, 1993, and reference therein]. The standoff distance of the magnetic pileup boundary (MPB) was calculated to be 1.2 R_M [*Trotignon et al.*, 1996]. MGS observations (made approximately halfway between solar min and solar max) put the bow shock standoff distance at about 1.6 R_M and the MPB standoff distance at 1.3 R_M [*Vignes et al.*, 2000]. These calculation involve many bow shock and MPB crossings and therefore are an average over different solar wind conditions.

3. SSMAs at Noon

[19] Figure 1 shows the solar wind density and temperature on the dayside at 1.1 R_m (or an altitude of 400 km) for cases A, B, D, and F (Table 2) when the SSMAs are located at noon. This altitude was chosen because the orbital altitude of the Mars Global Surveyor (MGS) satellite is approximately 400 km. Immediately one can see significant geographic variability in both the solar wind density and temperature in the vicinity of the magnetic anomalies. In fact, for all of the cases in Table 2, there is an order of magnitude variation in both the solar wind density and the solar wind temperature as a function of geographic location on the dayside. *Leblanc et al.* [2002] saw a similar geographic variation in their model of the flux of SEPs at an altitude of 200 km. To correlate the origin of the geographic variation in both the solar wind density and temperature at 400 km with the magnetic field geometry, Figure 2 shows magnetic field lines for three of the four cases in Figure 1. An additional case, case C, is shown in Figure 2b. In case C, the only change from nominal solar wind conditions (case A) is a rotation of the IMF direction.

[20] The cases studied can be classified into two groups. Cases B, C, D and H (Table 2) are a variation in a single solar wind parameter starting from quiet solar wind conditions (case A). This helps determine which parameters have the strongest influence on plasma flows in the Martian magnetosphere. Cases E, G, and F are variations in the solar wind conditions starting from an elevated solar wind density (case D) which would be associated with current day storm conditions or nominal solar wind conditions in the past.

3.1. Variations to Quiet Solar Wind Conditions

[21] In case A, the subsolar point of the bow shock is at 2 R_m (as measured from the center of the planet) and the subsolar point of the magnetic pileup boundary (MPB) forms at 1.6 R_m. When the solar wind speed is doubled (from case A to case B, Figures 1c and 1d), the solar wind density at 400 km is similar to that for nominal conditions (case A), both in geographic distribution and maximum and minimum values. In case B, the bow shock and MPB form at 1.9 R_m and 1.5 R_m, respectively. Therefore the solar wind density at 400 km in case B is roughly the same as in case A because the bow shock and MPB are still far enough away from the planet that the magnetic field geometry is roughly the same. The geographic distribution of the temperature in case B is also similar that in case A but the maximum temperature is on the order of 4 times larger than in case A, even though the temperature of the solar wind is the same. This increase in the temperature near the inner boundary is due to conservation of energy. The flow energy of the solar wind is converted into thermal energy near the inner boundary, and as energy goes as the square of the velocity, the thermal energy (and temperature) will increase by a

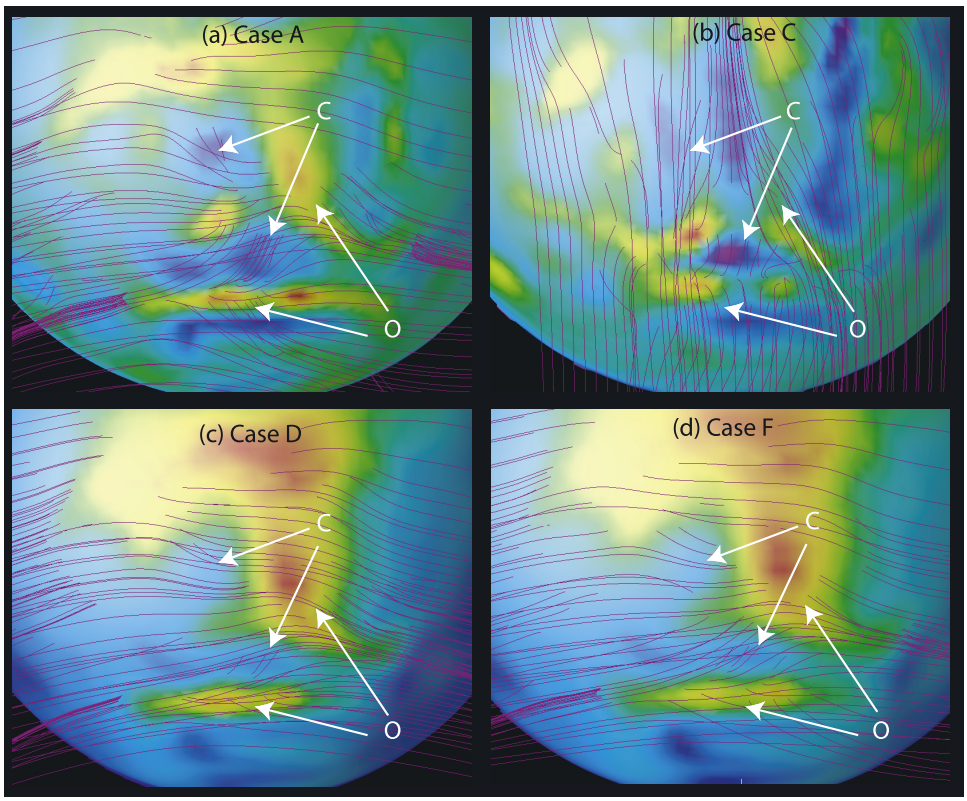

Figure 2. Magnetic field lines for cases (a) A, (b) C, (c) D, and (d) F and the solar wind density at an altitude of 400 km when the SSMAs are located at noon. The surface density plots for cases A, D, and F are identical to those in Figure 1. The color bar for the surface density for case C is the same as for case A. Examples of regions that remain closed for four cases are marked with "C," and regions that remain open are marked with "O".

factor of four in regions where the solar wind is funneled to the surface.

[22] Figure 2a shows that the regions of high solar wind density and temperature are associated with open field lines and the low-density/low-temperature regions are associated with closed field lines. Once the solar wind crosses the bow shock and enters the magnetosheath, the direction of the bulk flow switches from perpendicular to the magnetic field (as occurs outside the bow shock) to primarily parallel to the magnetic field at the MPB. Thus the plasma streamlines are similar to the magnetic field lines near the inner boundary. Wherever open field lines contact the inner boundary, hot solar wind plasma from the sheath or MPB can impact the surface. This is seen in MGS data. Analyzing data from many orbits, *Brain et al.* [2005] found that in regions with mostly radial magnetic field there was a statistically higher probability of measuring electron spectra with sheath-like characteristics. The data analyzed by *Brain et al.* [2005] also indicated that in some regions MGS measured electrons of ionospheric origin in 100% of the data sets. These regions protected from the solar wind are in roughly the same location as the closed field line regions in Figures 2a and 2b. To investigate how the regions of closed magnetic field lines respond to changes in the IMF, it was rotated 90° for nominal conditions (case C).

[23] Comparison of the solar wind density and temperature for case A and case C, shows that while the geographic pattern of the solar wind density and temperature changes when the IMF is rotated, the maximum values remain roughly the same in both cases. This is due to the fact that the bow shock and MPB form at the same location in both cases. While the magnetic field geometry is different, the magnetosphere has the same size. Therefore the temperatures of the plasma in the sheath region will be the same in both cases and the pileup of IMF in the magnetic pileup layer will be the same.

[24] However, even with geographic variability of the solar wind at 400 km, when the IMF is rotated, regions of open and closed magnetic field lines in the center of Figure 2a can be seen at the same location in Figure 2b. In Figure 2b the closed magnetic field (marked C) becomes more north-south aligned and the overall size of the regions does not remain constant, but the centers of the regions of closed field lines remain closed for the rotated IMF. This means that in these regions, the solar wind is almost completely deflected for both IMF configurations, and thus only ionospheric plasma will be present, in agreement with the analysis by *Brain et al.* [2005].

[25] In all the previous cases, the subsolar distance of the bow shock varied little with changes in the solar wind conditions. When the solar wind density was increased from nominal conditions by a factor of six (case A to case D), the bow shock and the MPB move closer to the surface, with the distance of the subsolar points at 1.6 R_m and 1.3 R_m

respectively. As a result, the peak solar wind and temperature at 400 km increases by a factor of 5 (Figures 1e and 1f). The MPB forms close enough that hotter plasma from the sheath can impact the inner boundary near the subsolar point.

[26] The above results indicate that, individually, fluctuations in the solar wind density will have the greatest influence on the amount of solar wind seen near the surface. Not only is the solar wind plasma in cusp-like regions hotter, it is more dense. High-speed streams only lead to hotter solar wind in the cusp regions, not more of it. With these results in mind, the solar wind parameters were again varied but the case with elevated solar wind density (case D) forming the baseline conditions.

3.2. Variations in Storm Conditions

[27] Increasing just the solar wind speed by a factor of two from nominal conditions lead to no increase in the peak solar wind density at 400 km and an increase in the solar wind temperature at 400 km that can be attributed to just conversion of kinetic energy to thermal energy. The solar wind conditions chosen in this parameter study suggest that this does not remain true when the solar wind density is already elevated above nominal conditions. When the solar wind speed is doubled while the solar wind density and IMF strength are held constant at 12 ions cm^{-3} and 2 nT, respectively (case D to E), the maximum solar wind density at 400 km increases from 5.5 ions cm^{-3} to 14 ions cm^{-3}. The maximum temperature in case E is 924 eV, more than 6 times that in case D, meaning the increase in not purely due to conversion of kinetic energy into thermal energy. This additional increase is due to the fact the the MPB forms essentially at the inner boundary in the vicinity of the subsolar point for case E. Of all of the cases listed in Table 2, the bow shock forms closest to planet in case E, with the subsolar point of the bow shock at 1.4 R_m, and the MPB at 1.1 R_m, or just above the inner boundary. Therefore the plasma around the subsolar point on the 400 km altitude map is hot sheath plasma. The solar wind plasma in the magnetic pileup region (MPR) inside the magnetosheath, is hotter than the solar wind but not as hot as the plasma in the sheath. These simulation results showing sheath plasma present at 400 km agree with measurements made by MGS during the Halloween 2003 storm event. During some intervals, the MPB was observed to move below 400 km altitude [*Crider et al.*, 2005]. The model results suggest that the high velocity of the solar wind, in conjunction with the elevated densities, during some intervals of this event, was integral to observing the presence of sheath plasma at or below 400 km.

[28] When the solar wind density is elevated, (case D) the magnetosphere is compressed. When the IMF strength is increased as well (from case D to case F, Figures 1g and 1h), the maximum density and temperature decrease. This is due to the fact that the bow shock and MPB move away from the planet, to 1.8 R_m and 1.5 R_m respectively, even though the total pressure of the solar wind increases. This is due to the nature of the pileup of IMF around the planet. As the IMF encounters the planet, it piles up on the dayside in the MPR. The MPB is the boundary between the magnetosheath and the MPR, forming the outer edge of the MPR. The ionopause forms the inner edge of the MPR. The IMF in the MPR slides around the planet at the terminators. Increasing the IMF strength leads to both a thicker MPR and increased magnetic field strengths in the MPR, as the IMF is limited in how fast it can slide around the planet. As the MPR thickens the ionopause moves closer to the surface but the MPB moves further away from the planet. This in turn pushes the magnetosheath, and hence the bow shock, away from the planet as well. Observational evidence for this behavior come from MGS measurements that showed increased magnetic field magnitudes in the MPR during the Halloween 2003 storm event [*Crider et al.*, 2005].

[29] When the solar wind density is elevated by an order of magnitude from nominal conditions (cases D-G), the regions of high solar wind density and temperature at 400 km all have a geographic distribution similar to that in Figures 1e–1h, regardless of the speed and IMF strength. In case G, the solar wind density is a factor of 20 greater than the nominal density and the IMF strength is increased by a factor of 3 from the nominal strength, while the solar wind speed is held constant. In this case the maximum solar wind density at 400 km increases to 30 ions cm^{-3}. The maximum temperature of 180 eV at 400 km in case G is comparable to that in case D, where only the solar wind density was increased from nominal conditions. However, the maximum temperature in case G is an order of magnitude larger than case F, where both the solar wind density and IMF strength were increased.

[30] This behavior is due to the fluctuation in the location of the bow shock and MPB among the cases D-G. Increasing the solar wind density (case A to D) pushes the bow shock closer to the surface, increasing the density and temperature of the solar wind at 400 km. The increase in temperature is indicative of the bow shock, and thus the sheath forming closer to the planet. Increasing the IMF strength on top of that (case D to F) causes the magnetic pileup region to thicken, pushing the MPB and thus the bow shock and sheath, region away from the surface, leading to a decrease in the solar wind density and temperature at 400 km. A further increase in the solar wind density (case F to G) pushes the bow shock closer to the surface again, causing the solar wind density and temperature to increase again.

[31] This behavior also points to reasons for the discrepancy between the average measured distance of the subsolar point for the bow shock and MPB and the values in case A, which are on the order of 25% larger. First, the average measured position will include measurements made during higher-density/higher-speed flows. Second, the model does not include the affects of pickup ions from the hot oxygen corona. Pickup ions from the corona will mass load the solar wind. The affect of this can be seen by looking at case D, where the subsolar distance for the bow shock and MPB match the average measured values. A mass density of 12 H^+ cm^{-3} is equivalent to a mixed wind with 2 H^+cm^{-3} and 0.6 O^+cm^{-3}.

[32] In the previous section it was shown that some regions of closed magnetic field lines remained closed for rotations of the IMF, which agreed with a statistical analysis of MGS data by *Brain et al.* [2005]. Also the "protected" regions in the model results are in the same vicinity as some seen in the data. This remains true for the more storm-like conditions with elevated solar wind densities. Regions of

Table 3. Loss and Precipitation Rates[a]

	Case A	Case B	Case C	Case D	Case H
Unmagnetized	2.6(O), 1.3(S)	4.8(O), 1.8(S)	2.6(O), 1.3(S)	5.8(O), 1.9(S)	2.3(O), 0.7(S)
SSMAs at noon	2.4(O), 1.3(S)	4.8(O), 1.7(S)	2.5(O), 1.3(S)	5.5(O), 1.9(S)	2.0(O), 0.8(S)
SSMAs at dusk	2.5(O), 1.3(S)	4.2(O), 1.6(S)	2.5(O), 1.3(S)	5.6(O), 1.9(S)	2.3(O), 0.7(S)
SSMAs at dawn	2.6(O), 1.3(S)	4.0(O), 1.7(S)	2.5(O), 1.3(S)	5.5(O), 1.8(S)	2.2(O), 0.7(S)
SSMAs at midnight	2.6(O), 1.3(S)	4.8(O), 1.8(S)	2.5(O), 1.3(S)	5.4(O), 1.9(S)	2.2(O), 0.9(S)

[a]Ionospheric loss and solar wind precipitation rates as function of planetary orientation. "O" is the loss rate of ionospheric O_2^+ in Cases A-D and ionospheric O^+ in Case H. "S" is the rate of solar wind precipitation into the ionosphere. All values are given in units of 10^{25} ions s^{-1}.

closed magnetic field lines seen in cases A and C (Figures 2a and 2b) shrink in overall size for the high solar wind density cases but do not completely disappear (Figures 2c and 2d).

[33] One difference with MGS observations is that during the Halloween 2003 storm, *Crider et al.* [2005] found the region around 50°–55°S and 160°E where the field lines are open and mostly radial for nominal solar wind conditions, became a region of closed field lines for storm conditions. The compression of the magnetosphere increased the horizontal component of the magnetic field in the MPR, meaning that the typically radial magnetic field in this region developed a large horizontal component, allowing closed field lines to form. Comparing the field line geometry between case A and cases D or F (Figures 2c and 2d), regions with open magnetic field geometry (examples are marked O) in case A remain so in cases D and F. The location indicated with the bottom most arrow is approximately 50°–55°S and 160°E. The solar wind conditions in cases D and F are similar to the times analyzed by *Crider et al.* [2005] in that the IMF remained mostly horizontal while the dynamic pressure increased from nominal conditions. There are a couple possible reasons for this discrepancy. First, the simulations are run with the equatorial plane aligned with the ecliptic plane, but during the Halloween 2003 storm, it was summer in the Martian southern hemisphere. Therefore the region described above was on the order of 20° closer to the ecliptic plane. Another possibility is resolution; the finest resolution of the simulations is 109 km, while MGS takes samples approximately every 2.5 km, and therefore the simulations may be missing small scale features that MGS can measure.

4. Ionospheric Loss Rates

[34] The results in the previous section indicate that the simulation results are in qualitative agreement with MGS observations of the response of the magnetosphere to storm conditions. The simulation results also indicate that an increase in solar wind precipitation occurs during storm conditions, potentially leading to strong heating of the ionosphere and a corresponding increase in the ionospheric loss rate. Furthermore, with the geographic variability caused by the magnetic anomalies, there is the possibility of significant variability in solar wind precipitation as a function of SSMA orientation. For example, when the SSMAs are on the night side, the solar wind will not have direct access to the surface through the cusp-like regions that are now on the nightside. With a decrease in solar wind precipitation at cusp-like structures around the SSMAs could come a decreased ionospheric loss rate as heating of the ionosphere by solar wind plasma is reduced. However, at the same time when the SSMAs are on the dayside, regions of closed magnetic field lines form that can protect regions from solar wind access.

4.1. Variations With SSMA Location

[35] To quantitatively assess the net affect of the SSMAs on the ionospheric loss rate, the simulations were run for each set of solar wind conditions listed in Table 2, with an unmagnetized Mars, the SSMAs at the noon and midnight meridians, and the SSMAs at the dawn and dusk terminators. Table 3 shows the ionospheric loss rates and the solar wind precipitation rates as a function of SSMA orientation for five of the cases in Table 2. The total flux is a function of the number density and velocity of each species, and is calculated over a surface far enough away from the planet in order to not be affected by local variations. The average ionospheric loss rate for nominal conditions (case A) is comparable to that determined from Phobos 2 measurement of 3×10^{25} ions s^{-1} [*Lundin et al.*, 1989].

[36] The results in Table 3 show that the ionospheric loss rate (O) and the solar wind precipitation rate (S) are essentially independent of the position of the magnetic anomalies relative to the incident direction of the solar wind. This remains true even for cases where the bow shock forms very close to the surface, such as cases D and E. *Leblanc et al.* [2002] found that the reduction in flux of SEPs to the surface in some regions was offset by magnetic field geometries in nearby regions that effectively funneled the deflected particles to the surface. Thus the presence of the anomalies did not change the net flux of SEPs to the surface. This appears to be true for the bulk flow of the solar wind as well.

[37] Only in case B does the ionospheric loss rate appear to vary with SSMA orientation. The maximum magnitude of the fluctuations between orientations is 0.8×10^{25}, comparable to the variation between some cases with different solar wind conditions (case E and F, for example). Case B is unusual in that near the end of the simulation run, reconnection-like changes in the magnetic field driven by Hall currents occurred in the tail for more than one of the SSMA orientations. This also occurred, to a lesser extent, in case E, where the solar wind velocity was also set to 800 km/s. The magnitude of the variation between orientations in case E is 0.5×10^{25}. Reconnection occurring close to the planet, where the oxygen density is higher has the potential to increase the ionospheric loss rate by accelerating bound oxygen ions down tail, to be lost from the system. This will also introduce a time variability to the ionospheric oxy-

Table 4. Averaged Loss and Precipitation Rates[a]

	Ionospheric Outflow	Solar Wind Precipitation
Case A: Nominal	2.5	1.3
Case B: Fast Solar Wind	4.5	1.7
Case C: Nominal Bz	2.5	1.3
Case D: Elevated solar wind density	5.6	1.9
Case E: Elevated density and speed	7.6	2.4
Case F: Large speed, density and IMF	8.7	3.0
Case G: Large speed and IMF, very high density	12	4.9
Case H: Nominal light mass ionosphere	2.2	0.75

[a]Ionospheric outflow and solar wind precipitation rates averaged over all five of the anomalous magnetic field configurations. All values are given in units of 10^{25} ions s^{-1}.

gen outflow calculation that can lead to variations between different simulation runs. Analyzing observations of auroral-like electron spectra measured by MGS, *Brain et al.* [2006] concluded that reconnection is required to observe such accelerated electrons. These simulation results suggest that high-speed flows in the solar wind enhance the likelihood of reconnection occurring. A more detailed analysis of simulated reconnection in the tail is left to another paper as it does not fit within the scope of this paper.

4.2. Variations With Solar Wind Conditions

[38] As the magnetic field orientation does not appear to play a large roll in controlling net loss rate of the ionosphere in most of the cases studied, the ionospheric outflow and solar wind precipitation rates are averaged over all five anomalous magnetic field configurations for all the cases in Table 2. These averages are shown in Table 4. From these values, the variation of ionospheric loss rate as a function of solar wind condition can be determined.

[39] The results show that the elevated solar wind pressures associated with storm conditions can be a strong driver of ionospheric loss, while the solar wind precipitation rates change by a lesser extent. A doubling in the solar wind speed (case A to case B) increases the ionospheric loss rate by 80%, while a 6 fold increase in the solar wind density (case A to case D) increases the loss rate by 120%. However, the solar wind precipitation rates increase by only 30% and 46% respectively. This indicates that one or more processes other than direct heating by solar wind precipitation has a significant influence on ionospheric loss.

[40] This large increase in the ionospheric loss rate for fast solar wind speeds does not occur when the magnetosphere is already compressed. Doubling the solar wind velocity when the magnetosphere is compressed due to high solar wind densities (case D to case E) increase the ionospheric outflow rate by only 40%, instead of the 80% increase seen when the solar wind velocity doubles at nominal solar wind densities (case A to case B). This may be due to limitations set by the boundary conditions though because the solar wind precipitation rate increases by about 30%, which is comparable to the increases seen for the larger magnetospheres in cases B and D. The simulation has static, not dynamic, boundary conditions at the inner boundary. The inner boundary can act as both a source and a sink for particles but with a fixed temperature and density that does not increase either globally or locally with increased solar wind precipitation, this will limit the effective source rate.

[41] Storm events can play a significant role in atmospheric loss at the Earth. Observations at the Earth have shown that the flux of oxygen out of the Earth's ionosphere can increase by up to three orders of magnitude during cloud events while the proton flux only increases by an order of magnitude [*Yau and Andre*, 1997]. Multifluid simulations for the response of the Earth's magnetosphere to storms [*Winglee et al.*, 2002] showed that storm conditions would increase the ionospheric oxygen outflow rate by about a factor of 5 when the simulations were run with static boundary conditions. Allowing for dynamic boundary conditions increased the outflow rate by another order of magnitude, to a value much closer to those observed. Both the fact that the ionospheric loss rate does not increase as dramatically with solar wind speed when the magnetosphere is already compressed and that the simulations show at most an order of magnitude increase in the loss of oxygen from the ionosphere, suggest that it is necessary to include dynamic boundary conditions at Mars that allow for a response by the ionosphere due to solar wind forcing. This could lead to a significant increase in the ionospheric loss rates for the same precipitation rates.

[42] Another indication that processes other than direct heating of the ionosphere have a significant influence on the loss rates comes from looking at the oxygen temperature near the inner boundary. O_2^+ is only marginally gravitationally bound at Mars for ionospheric temperatures of 3000 K, or 0.3 eV. This temperature is equivalent to a thermal velocity of 1525 m/s, 30% of the escape velocity, and therefore a substantial fraction is already being lost even under nominal solar wind conditions. The peak oxygen temperature at 400 km is approximately 1 eV in case A, and increases to approximately 6 eV when the solar wind density is increased in case D and 35 eV when the solar wind speed is also increased in case E, both of which are well above the temperature of 4.2 eV for which O_2^+ will escape due to thermal velocity alone. When the IMF is increased in addition to the solar wind speed and density in case F, the maximum oxygen temperature is slightly less than 1 eV, suggesting that the loss rate should decrease but the O_2^+ loss rate increases further.

[43] One of the processes involved in heating can be determined by comparing loss and precipitation rates in case A and B. In both cases the bow shock and MPB form at the same location. The solar wind precipitation rates for the two cases is comparable, but the oxygen loss rate is double in case B. Doubling of the solar wind speed means the

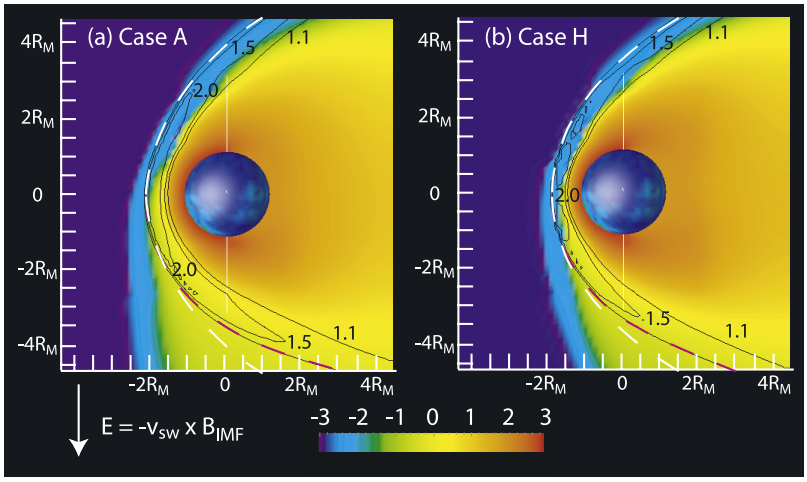

Figure 3. Solar wind and ionospheric density in the the asymmetric (xz) plane for cases (a) A and (b) H. The color contours show the log of ionospheric density. The black contour lines indicate the solar wind density relative to the incident solar wind density and the position of the bow shock. The white dashed curve is symmetric about the equator and traces the outer edge of the bow shock in the northern hemisphere in both Figures 3a and 3b. The pink dashed curve traces the outer edge of the bow shock in the southern hemisphere. The convection electric field points in the same direction in both Figures 3a and 3b.

cyclotron radius of the pickup ions also doubles, and these ions can then flow past the planet, being lost to the solar wind. Pickup playing an important role in ionospheric loss also explains why loss rates can double for some solar wind conditions, while the solar wind precipitation rate only increases by ~50%. It is a nonlinear mechanism. Pickup of ionospheric ions by the solar wind occurs at Mars and can be captured by the model. The effect of pickup can be further quantified by varying the mass of the ionospheric species while keeping the solar wind conditions constant.

[44] In cases A and H the solar wind conditions are identical, the only difference is that in case H, the mass of the ionospheric ion is reduced by a factor of 2. The oxygen loss rate and solar wind precipitation rate are not identical. The oxygen loss rate is on the order of 10% smaller in case H while the solar wind precipitation rate is on the order of 40% smaller. This is not due to the bow shock and MPB forming further from the surface in case H. The subsolar distance of the bow shock and MPB in case H is closer than in case A, at 1.8 R_m and 1.5 R_m respectively, because the O^+ ionosphere presents less of an obstacle in terms of mass.

[45] The decrease in solar wind precipitation in case H comes from both the mass of the ionospheric component and the fact that the model can capture ion cyclotron effects. Figure 3 shows the ionospheric and solar wind densities in the plane perpendicular to the IMF (i.e. the xz plane) for cases A and H. Ionospheric ions are accelerated in the direction of the convection electric field, and they are picked up by the solar wind. As ionospheric ions are pulled into the solar wind, solar wind ions must be pulled toward the planet in order to maintain charge neutrality (as this process is driven by the electric field). Therefore the bow shock is asymmetric, forming closer to the planet on the side where the pickup region forms. This results in the formation of a region of ionospheric ions outside of the bow shock, and the size of this region is a function of the ion cyclotron radius. The larger the ion mass (or velocity), the larger the pickup region. The lighter mass of the ionospheric constituent in case H means that it has a smaller cyclotron radius. As a result the pickup region outside the bow shock is smaller than in case A and the asymmetry of the magnetosphere is smaller as well (Figures 3a and 3b). This can be quantified in a couple of ways.

[46] In case A (Figure 3a), the outer edge of the bow shock forms at 4.2 R_m above the pole in the northern hemisphere and 3.6 R_m above the pole in the southern hemisphere. In case H (Figure 3b), the distances are 3.7 R_m and 3.4 R_m respectively. The asymmetry can also be seen by comparing the white and pink curves in the southern hemisphere in both Figures 3a and 3b. The white curve indicates where the outer edge of the bow shock would form in the southern hemisphere if it was symmetric with the northern hemisphere. The pink curve indicates the actual location of the outer edge of the bow shock. Measuring at the bottom edge of Figure 3, the separation between the two curves is approximately 1.5 R_m in case H and 2.0 R_m in case A. Comparing the distance between the white dotted curve and the outer edge of the pickup region in Figures 3a and 3b, the separations is approximately 3.5 R_m in case A and 2.5 R_m in case H (near the bottom edge of Figure 3). With a smaller pickup region in case H, less ionospheric material is pulled into the solar wind and less solar wind is pulled toward the planet, ergo less ionospheric loss and less solar wind precipitation.

[47] However, neither direct heating nor pickup explains why the ionospheric loss rate in case F is greater than the loss rate in case E. The peak O_2^+ temperature in case F is approximately six times smaller than case E at 400 km and the IMF strength is three times larger than in case E, meaning the ion cyclotron radius is smaller, thus the pickup region in case F is smaller. Both of these characteristics suggest the ionospheric loss rate in case F should be smaller

than in case E. The crucial difference is that while the stronger IMF means the pickup region will be smaller, the plasma sheet in the tail will be considerably bigger. Analysis of Phobos 2 data by *Verigin et al.* [1991b] showed that escapes rates are a product of the plasma sheet diameter and thickness. The highly compressed magnetosphere in case E leads to one of the smallest plasma sheets of all the cases studied (only the plasma sheet in case H is smaller). In contrast, the plasma sheet in case F is the largest of all the cases studied. Case G has the largest outflow rate of all the cases because the plasma sheet size is only slightly smaller than the plasma sheet in Case F, while the pickup region in case G is significantly bigger than in case F. This highlights the important role that pickup plays in ionospheric loss at Mars. Without pickup, the loss rate in case E would be comparable to that for nominal solar wind conditions. Pickup increases the ionospheric loss rate by approximately a factor of three.

5. Conclusions

[48] Three-dimensional multifluid simulations of the solar wind interaction with Mars for quiet to storm conditions indicate that the loss rate of ionospheric oxygen can increase by an order of magnitude for storm-like conditions. The computed outflow rates for nominal solar wind conditions agree with that measured by Phobos 2. Comparison of simulations of the solar wind interaction with Mars for storm-like conditions with data measured by MGS during the Halloween 2003 storm indicate qualitative agreement with the response of the magnetic pileup layer to changes in the solar wind conditions. Difference between the model results and satellite data may be due to difference in exact solar wind conditions. As there is no satellite monitoring the solar wind conditions at Mars, the conditions can only be estimated from data measured inside the magnetosphere.

[49] The simulations indicate that the composition of the ionosphere effects both the solar wind precipitation rate and the ionospheric loss rate as both are affected by pickup. Decreasing the mass of the ionospheric component, reduces the size of the pickup region and leads to a reduction of solar wind precipitation and ionospheric loss. This is important for studying the evolution of the Martian atmosphere as it may have been dominated by lighter species in the distant past. It also means that pickup processes are important when considering the effects of solar storm on loss rates. Changes in the solar wind that lead to increases in ionospheric pickup will increase the loss rates over what would be estimated from the size of the plasma sheet. Furthermore, as ionospheric loss rates and solar wind precipitation rates will not change by equal amounts, loss rates cannot be estimated from precipitation rates. It also means that loss rates vary nonlinearly with changes in the solar wind conditions.

[50] The results also show that the magnetic anomalies do not strongly modulate either the solar wind precipitation rate or the ionospheric oxygen loss rate for most solar wind conditions, even though the anomalies lead to significant geographic variation in the solar wind precipitation. However, the results may be limited by the resolution of the simulations. The resolution is sufficient to capture ionospheric escape but local variations in the ionospheric scale height due to the magnetic anomalies are limited to the smallest grid resolution of 100 km, which may be the reason that the loss rates vary little with planetary orientation. With higher resolution, smaller scale heights may develop allowing for more extensive local density enhancements in ionospheric oxygen. The next step in the simulations will be to include high-resolution gridding over the SSMAs.

[51] The next step will also include dynamic boundary conditions at the inner boundary to allow for variations in the ionosphere that will occur with increased precipitation during a storm. In the simulations, the temperature, density and conductivity of the inner boundary is held constant throughout the simulation and is not geographically variable, other than the day-night asymmetry. In reality, as more solar wind plasma precipitates into the ionosphere, the ionosphere will be heated and the conductivity will change. This can lead to greater outflow rates. Thus the loss rates predicted for storm conditions determined from these simulations are most likely a lower bound.

[52] Studying the response of the Martian ionosphere to storm conditions is useful in its own right but it also has astrobiological implications, as at least some of the water, and maybe a large portion of the CO_2, present on an young Mars escaped to space. What is not well constrained is how quickly Mars could have lost water and atmosphere to space once the global dynamo ceased. The nominal conditions for the early Sun are comparable enough to current day storm conditions that storms can be used as analogs for earlier Sun conditions. Studying the response of the Earth's magnetosphere and the variation in ionospheric loss rates during solar storms has shown that changes are typically nonlinear. The results in this paper indicate that the same is true at Mars. Therefore using current day storm conditions as early Sun analogs provides a means to validate the models against data and increases the confidence in predictions made for a time when liquid water is thought to have been present on the surface of Mars.

[53] **Acknowledgments.** This work was funded by NASA Mars Fundamental grant NNG05GLL9G.

[54] Wolfgang Baumjohann thanks the reviewers for their assistance in evaluating this paper.

References

Acuna, M., et al. (2001), Magnetic field of Mars: Summary of results from the aerobraking and mapping orbits, *J. Geophys. Res.*, *106*, 23,403–23,417.

Brain, D. A., and B. M. Jakosky (1998), Atmospheric loss since the onset of the Martian geologic record: Combined roll of impact erosion and sputtering, *J. Geophys. Res.*, *103*, 22,689–22,694.

Brain, D. A., et al. (2005), Variability of the altitude of the Martian sheath, *Geophys. Res. Lett.*, *32*, L18203, doi:10.1029/2005GL023126.

Brain, D. A., et al. (2006), On the origin of aurora on Mars, *Geophys. Res. Lett.*, *33*, L01201, doi:10.1029/2005GL024782.

Brecht, S. (1997a), Hybrid simulations of the magnetic topology of Mars, *J. Geophys. Res.*, *102*, 4743–4750.

Brecht, S. (1997b), Solar wind proton deposition into the Martian atmosphere, *J. Geophys. Res.*, *102*, 11,287–11,294.

Burlaga, L., et al. (1998), A magnetic cloud containing prominence material: January 1997, *J. Geophys. Res.*, *103*, 277–285.

Cain, J. C., et al. (2003), An n = 90 internal potential function of the Martian crustal magnetic field, *J. Geophys. Res.*, *108*(E2), 5008, doi:10.1029/2000JE001487.

Crider, D. H., et al. (2005), Mars Global Surveyor observations of the Halloween 2003 solar superstorm's encounter with Mars, *J. Geophys. Res.*, *110*, A09S21, doi:10.1029/2004JA010881.

Dennis, B. R. (1988), Solar flare hard X-ray observations, *Sol. Phys.*, *118*, 49–94.

Fox, J. L. (1997), Upper limits to the outflow of ions at Mars: Implications for atmospheric evolution, *Geophys. Res. Lett.*, *24*, 2901–2904.
Hanson, W. B., et al. (1977), The Martian ionosphere as observed by the Viking retarding potential analyzers, *J. Geophys. Res.*, *82*, 4351–4363.
Harnett, E. M., and R. M. Winglee (2005), Three-dimensional fluid simulations of plasma asymmetries in the Martian magnetotail caused by the magnetic anomalies, *J. Geophys. Res.*, *110*, A07226, doi:10.1029/2003JA010315.
Harnett, E. M., et al. (2005), Pluto's magnetosphere: A comparison between 3D hybrid and 3D multi-fluid simulation results, *Geophys. Res. Lett.*, *32*, L19104, doi:10.1029/2005GL023178.
Jakosky, B. M., and R. J. Phillips (2001), Mars' volatile and climate history, *Science*, *412*, 237–244.
Kallio, E., and P. Janhunen (2002), Ion escape from Mars in a quasi-neutral hybrid model, *J. Geophys. Res.*, *107*(A3), 1035, doi:10.1029/2001JA000090.
Kallio, E., and H. Koskinen (1999), A test particle simulation of the motion of oxygen ions and solar wind protons near Mars, *J. Geophys. Res.*, *104*, 557–579.
Kallio, E., et al. (1995), Oxygen outflow in the Martian magnetotail, *Geophys. Res. Lett.*, *22*, 2449–2453.
Kar, J., et al. (1996), On the outflow of O_2^+ ions at Mars, *J. Geophys. Res.*, *101*, 12,747–12,752.
Knudsen, W. C. (1992), The Venus ionosphere from in situ measurements, in *Venus and Mars: Atmospheres, Ionospheres and Solar Wind Interactions*, *Geophys. Monogr. Ser.*, vol. 66, edited by J. G. Luhmann et al., pp. 237–263, AGU, Washington, D. C.
Lammer, H., et al. (2003), Loss of water from Mars: Implications for the oxidation of the soil, *Icarus*, *165*, 9–25, doi:10.1016/S0019-1035(03)00170-2.
Leblanc, F., et al. (2002), Some expected impacts of a solar energetic particle event at Mars, *J. Geophys. Res.*, *107*(A5), 1058, doi:10.1029/2001JA900178.
Luhmann, J. G., and J. U. Kozyra (1991), Dayside pickup oxygen precipitation at Venus and Mars: Spatial distributions, energy deposition and consequences, *J. Geophys. Res.*, *96*, 5457–5467.
Luhmann, J. G., et al. (1992), Evolutionary impact of sputtering on the Martian atmosphere by O^+ pickup ions, *Geophys. Res. Lett.*, *19*, 2151–2154.
Lundin, R., et al. (1989), First measurements of the ionospheric plasma escape from Mars, *Nature*, *341*, 609–612.
Lundin, R., et al. (1990), ASPERA/Phobos-2 measurements of the ion outflow from the Martian ionosphere, *Geophys. Res. Lett.*, *17*, 873–876.
Lundin, R., et al. (2004), Solar wind-induced atmospheric erosion at Mars: First results from ASPERA-3 on Mars Express, *Science*, *305*, 1933–1936.
Ma, Y., et al. (2002), 3D multi-species MHD studies of the solar wind interaction with Mars in the presence of crustal fields, *J. Geophys. Res.*, *107*(A10), 1282, doi:10.1029/2002JA009293.
Ma, Y., et al. (2004), Three-dimensional, multispecies, high resolution MHD studies of the solar wind interaction with Mars, *J. Geophys. Res.*, *109*, A07211, doi:10.1029/2003JA010367.
Mitchell, D. L., et al. (2001), Probing Mars' crustal magnetic field and ionosphere with the MGS electron reflectometer, *J. Geophys. Res.*, *106*, 23,419–23,438.
Nagy, A. F., and T. E. Cravens (1988), Hot oxygen atoms in the upper atmosphere of Venus and Mars, *Geophys. Res. Lett.*, *15*, 433–435.
Ness, N. F., et al. (2000), Effects of magnetic anomalies discovered at Mars on the structure of the Martian ionosphere and solar wind interaction as follows from radio occultation experiments, *J. Geophys. Res.*, *105*, 15,991–16,004.
Newkirk, G., Jr. (1980), Solar variability on time scales of 10^5 years to $10^{9.6}$ years, *Geochim. Cosmochim. Acta Suppl.*, *13*, 293–320.
Ribas, I., et al. (2005), Evolution of the solar activity over time and effects on planetary atmospheres. I. High-energy irradiances (1–1700A), *Astrophys. J.*, *622*, 680–694.
Richardson, J. D., et al. (2005), Propagation of the October/November 2003 CMEs through the heliosphere, *Geophys. Res. Lett.*, *32*, L03S03, doi:10.1029/2004GL020679.
Rosenbauer, H., et al. (1989), Ions of Martian origin and plasma sheet in the Martian magnetosphere: Initial results from the TAUS experiment, *Nature*, *341*, 612–615.
Shinagawa, H., and T. E. Cravens (1989), A one-dimensional multispecies magnetohydrodynamic model of the dayside ionosphere of Mars, *J. Geophys. Res.*, *94*, 6506–6516.
Skoug, R. M., et al. (2004), Extremely high speed solar wind: 29–30 October 2003, *J. Geophys. Res.*, *109*, A09102, doi:10.1029/2004JA010494.
Smith, E. P., and D. M. Gottlieb (1974), Solar flux and its variations, *Space Sci. Rev.*, *16*, 771–802.
Trotignon, J. C., et al. (1993), Position and shape of the Martian bow shock: The Phobos-2 plasma wave system observations, *Planet. Space Sci.*, *41*, 189–198.
Trotignon, J. C., et al. (1996), Solar wind measurements near Mars and their implications in the Red Planet environment, *Planet. Space Sci.*, *44*, 117–127.
Tsyganenko, N. A., and M. I. Sitnov (2005), Modeling the dynamics of the inner magnetosphere during strong geomagnetic storms, *J. Geophys. Res.*, *110*, A03208, doi:10.1029/2004JA010798.
Verigin, M. I., et al. (1991a), On the problem of the Martian atmosphere dissipation: Phobos-2 TAUS spectrometer results, *J. Geophys. Res.*, *96*, 19,315–19,320.
Verigin, M. I., et al. (1991b), Ions of planetary origin in the Martian magnetosphere (Phobos-2/Taus experiment), *Planet. Space Sci.*, *39*, 131–137.
Vignes, D., et al. (2000), The solar wind interaction with Mars: Locations and shapes for the bow shock and the magnetic pile-up boundary from the observations of the MAG/ER experiment onboard Mars Global Surveyor, *Geophys. Res. Lett.*, *27*, 49–52.
Winglee, R. M. (2004), Ion cyclotron and heavy ion effects on reconnection in a global magnetotail, *J. Geophys. Res.*, *109*, A09206, doi:10.1029/2004JA010385.
Winglee, R. M., et al. (2002), Global impact of ionospheric outflows on the dynamics of the magnetosphere and cross-polar cap potential, *J. Geophys. Res.*, *107*(A9), 1237, doi:10.1029/2001JA000214.
Wood, B. E., et al. (2002), Measured mass-loss rates of solar-like stars as a function of age and activity, *Ap. J.*, *574*, 412–425.
Yau, A. W., and M. Andre (1997), Source of ion outflow in the high latitude ionosphere, *Space Sci. Rev.*, *80*, 1–25, doi:10.1023/A:1004947203046.
Zhang, J., et al. (2006), A statistical comparison of solar wind sources of moderate and intense geomagnetic storms at solar minimum and maximum, *J. Geophys. Res.*, *111*, A01104, doi:10.1029/2005JA011065.
Zhang, M. H. G., et al. (1993), The ancient oxygen exosphere of Mars: Implications for atmosphere evolution, *J. Geophys. Res.*, *98*, 10,915–10,923.

E. M. Harnett and R. M. Winglee, Department of Earth and Space Sciences, Box 351310, University of Washington, Seattle, WA 98195-1310, USA. (eharnett@ess.washington.edu; winglee@ess.washington.edu)